Liquid–Liquid Two-Phase Flow in Pore Array Microstructured Devices for Scaling-Up of Nanoparticle Preparation

Shaowei Li, Jianhong Xu, Yujun Wang, and Guangsheng Luo
Dept. of Chemical Engineering, The State Key Laboratory of Chemical Engineering, Tsinghua University, Beijing 100084, China

DOI 10.1002/aic.11945

Nanoparticles have been produced by a T-junction microchannel device in our previous work (Li et al., Langmuir. *2008;24:4194-4199). As a scaling-up strategy, pore array microstructured devices were designed to prepare nanoparticles in this article. H_2SO_4 and $BaCl_2$, respectively, in two phases to form $BaSO_4$ nanoparticles was used as a test system. The characteristics of a well controlled liquid–liquid two-phase flow in the pore array microstructured devices were presented. Nanoparticles with small size and good dispersibility were produced through drop or disk flows in the microstructured devices. The influence of mass transfer and chemical reaction on interfacial tension and flow patterns was discussed based on the experiments. Meanwhile, the effect of the two phase flow patterns on the nanoparticle size was discussed. It was found that the increase of the amount of mass transfer and chemical reaction could change the flow patterns from disk flow to drop flow. The droplet diameter could be changed in a wide range. Flow patterns could be distinguished based on the measured interfacial tension in different concentrations. The prepared nanoparticles were ranged from 10 nm to 30 nm. Apparently the particle size was decreased with the increase of the droplet size in both the drop flow region and the disk flow region whereas it had a reverse trend in the transition region.* *AIChE J,* 55: 3041–3051, 2009

Keywords: drop, mass transfer, microstructure, multiphase flow, particle formation, scale-up

Introduction

Recently, the rapid development of microreaction and micromixing technology has led to a considerable variety of microfluidic devices. These devices have been used in many fields for its high efficiency, safety, repeatability, and facile controllability.[1–21] In particular, significant advances have been made in the use of microfluidic devices for controlling the multiphase flow. Well controlled multiphase flows in microdevices have the advantages of large interfacial area, short transfer distance, and fast mixing performance, which can reduce mass transfer limitations to achieve much better performances relative to conventional scale systems.[22] Thus, well controlled multiphase flows in microdevices have been widely used in chemical reaction,[3–5] liquid–liquid extraction,[6–8] biological analysis,[9] crystallization,[10] polymer synthesis,[11–14] structural material preparation,[15–17] and nanoparticle synthesis.[18–21,23] Especially, in nanoparticle synthesis, particle size controlling is just one of the key issues in the production of nanoparticles because many properties of the solid particles are sensitive to the particle size and particle size distribution.[24] The drops or plugs flow can provide

---

Correspondence concerning this article should be addressed to G. Luo at gsluo@tsinghua.edu.cn

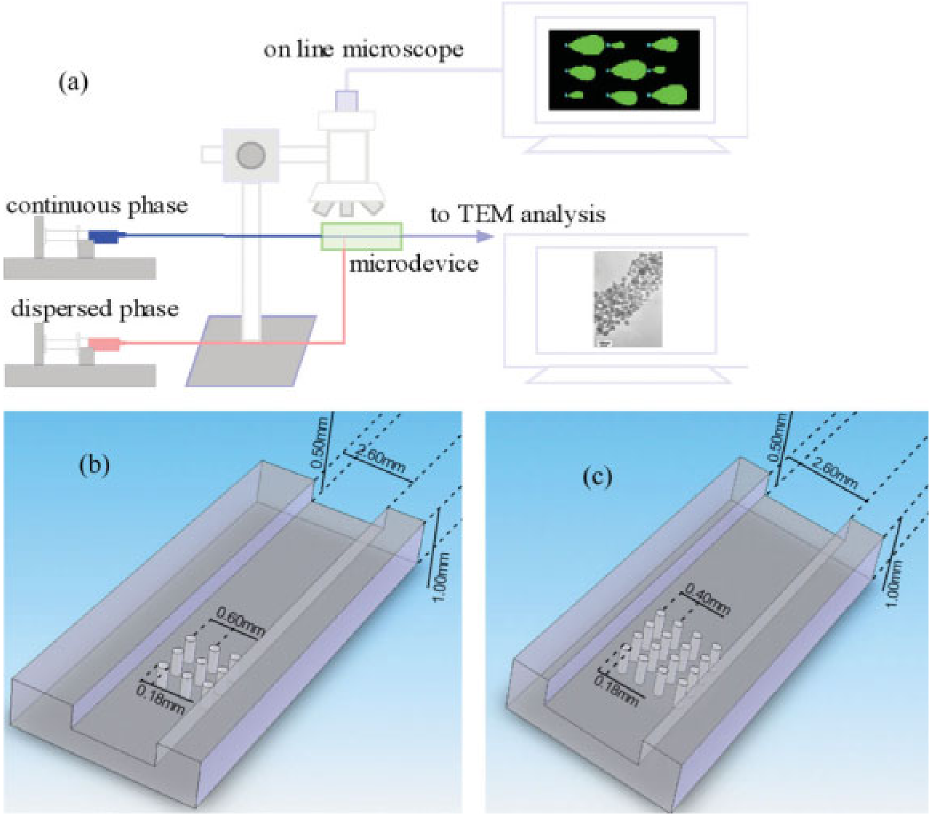

Figure 1. The experimental setup for nanoparticle preparation.

(a) Flow chart for the experiments; (b) Inner 3D structure of the microstructured device; (c) Sizes of the inner structure (The pore array is alternatively 3 × 3 or 4 × 4). [Color figure can be viewed in the online issue, which is available at www.interscience.wiley.com.]

high mixing efficiency which is very important in particle size controlling.[25–30] Moreover, well controlled multiphase flows can also prevent a liquid from direct contact with microchannel walls and thereby eliminate or reduce undesired clogging of channels due to deposition of material on wall surfaces.[22,23]

For large scale production processes, it is highly required to scale up the microdevices. A feasible strategy is fabricating numbers of branch channels as an array vertical to one main channel.[31,32] As a variation, micro-pore array fabricated in a channel also belongs to this strategy. The droplet formation process in the pore array microstructured device with different types of pores has been researched.[33–36] However, application in this kind of devices has been little reported. The mass transfer and reaction in the devices have been little researched either.

In our previous work, $BaSO_4$ nanoparticles have been produced by two-phase flow in a T-junction microchannel device. Mass transfer and reaction effect on the flow patterns has been researched. Particle size influencing factors have also been investigated.[37] Following the scaling up strategy mentioned earlier, and also as an application exploration of the pore array microstructured device, we designed a new structured microdevice with several pores and investigated the characteristics of liquid–liquid two-phase flow with a swarm of droplets in the microdevice. A system of H_2SO_4 and $BaCl_2$, respectively, in two phases to form $BaSO_4$ nanoparticles was used as a probe to characterize the micro-scale two-phase flow. The influence of mass transfer and chemical reaction on interfacial tension and two-phase flow was investigated. Meanwhile, the effects of the operation conditions and the droplet size on the particle size was also investigated and discussed.

Experimental

Figure 1 shows the experimental setup. Nanoparticles were produced in a pore array microstructured device. The main structure of the device (as shown in Figures 1b, c) was fabricated on a polymethyl methacrylate (PMMA) plate (50 × 20 × 1 mm) using micromachining. The sizes of the inner structure were shown in the figure. The main channel dimensions were 2.60 × 0.50 mm (width × height). The pore diameter was 0.18 mm. The length of the pore channel was 0.5 mm. The distance between two adjacent pores was 0.60 mm for the 3 × 3 array and 0.40 mm for the 4 × 4 array. The microfluidic device was sealed using other two PMMA plates (50 × 20 × 1 mm) by a self-developed bonding technique. Two microsyringe pumps and two gastight microsyringes were used to pump the two phases into the microstructured device, respectively.

Butyl alcohol solutions with sulfuric acid concentration of 0.05, 0.1, 0.2, 0.4, and 0.8 mol/l were used as the continuous phase. Aqueous solutions with barium chloride concentration of 0.05, 0.1, 0.2, 0.4, and 0.8 mol/l were used as the dispersed phase. As the contact angle for water and PMMA in

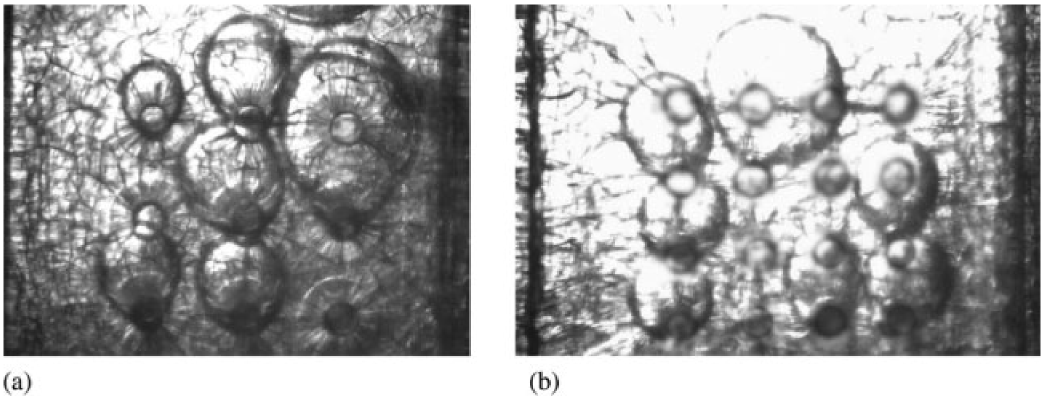

Figure 2. Droplet formation through the pore array.

(a) $Q_c = 500$ μl/min, $Q_d = 250$ μl/min, $C_c = 0.05$ mol/l, $C_d = 0.4$ mol/l. (b) $Q_c = 500$ μl/min, $Q_d = 350$ μl/min, $C_c = 0.05$ mol/l, $C_d = 0.4$ mol/l.

the ambience of butyl alcohol is about 150°, droplets of aqueous solution were formed by the crossflowing rupture in the main channel. Because barium chloride can not be dissolved in butyl alcohol, the reaction of sulfuric acid with barium chloride took place in the droplet when sulfuric acid diffused through the interface and nanoparticles of barium sulfate were produced.

A microscope at magnifications from 20× to 200× with a high-speed CCD video camera was used to capture the droplet images. The images were recorded at a frequency of 600 images/s and then analyzed using a custom-made image-analysis software to obtain the droplet size. About 200 droplets were measured for every operation condition and the Sauter mean diameter was calculated to represent the droplet size. The produced nanoparticles were characterized directly by TEM pictures on JEM2010 (Japan) and the particle size was analyzed using the TEM pictures. The transverse lengths of about 400 particles were measured for every operation condition and the mean value was used to represent the particle size.

Results and Discussion

Pore activity

As shown in Figure 2, where Q_c and Q_d are, respectively, the flow rate of the continuous phase and the dispersed phase, C_c and C_d are, respectively, the concentration of the continuous phase and the dispersed phase, not all of the pores are active in some experimental conditions. It can be found out that the fluid does not pass through all pores simultaneously. Some of the pores do not work, which is denoted as the inactive pores. The inactive pores are random and are alterable when some disturbance occurs, which is quite frequent in a practical process. For quantitative investigation, we counted the active pore percentage in different conditions. Figure 3 shows the active pore percentage varying with the apparent flow velocity of the dispersed phase, which is defined as

$$u_{\mathrm{d}}^{(\mathrm{a})} = \frac{Q_{\mathrm{d}}}{nA_{\mathrm{p}}} = \frac{4Q_{\mathrm{d}}}{n\pi d_{\mathrm{p}}^2}, \tag{1}$$

where d_p is the pore diameter. From Figure 3, we could see that the active pore percentage increases with the apparent flow velocity linearly until it reaches 100%. The linear relation could be expressed as

$$u_{\mathrm{d}}^{(\mathrm{a})} = u_{\mathrm{d}}^{(\mathrm{c})}\eta \tag{2}$$

where $u_{\mathrm{d}}^{(\mathrm{c})}$ is a constant. We could get the value of $u_{\mathrm{d}}^{(\mathrm{c})}$ by line fitting using the data in Figure 3. It is ~0.021 m/s. We will see in the following text that $u_{\mathrm{d}}^{(\mathrm{c})}$ is the so-called critical flow velocity of the dispersed phase.

The active pore percentage could be explained through the comparing between the droplet formation pressure and the capillary pressure. The droplet formation pressure is caused by the pore resistance and the interfacial tension of the droplet surface. The pore resistance could be expressed by the sum of Hagen-Poiseuille's resistance

$$R_{\mathrm{HP}} = \frac{128 l_{\mathrm{p}}}{\pi d_{\mathrm{p}}^4}, \tag{3}$$

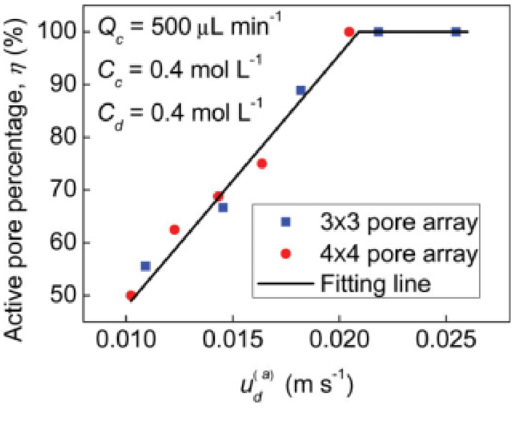

Figure 3. The active pore percentage varying with the apparent flow velocity of the dispersed phase.

[Color figure can be viewed in the online issue, which is available at www.interscience.wiley.com.]

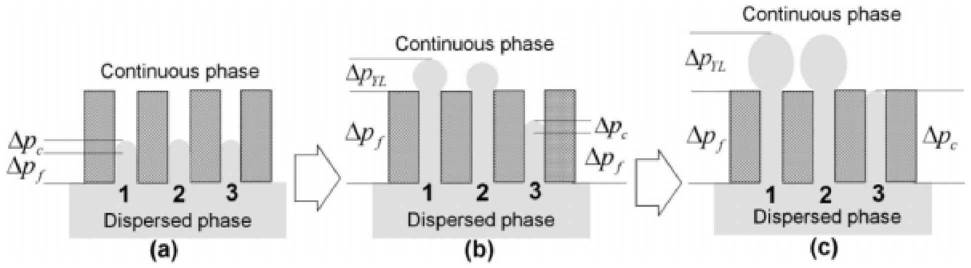

Figure 4. Pressures in the drop formation process.

which is due to the friction of the pore channel, and Sampson's resistance

$$R_{\mathrm{S}} = \frac{24}{d_{\mathrm{p}}^3}, \tag{4}$$

which describes the entrance effect adds to the resistance of the pore. Therefore, the pore resistance caused pressure could be expressed by the following equation[33,38]

$$\Delta p_{\mathrm{f}} = R_{\mathrm{HP+S}} \mu_{\mathrm{d}} u_{\mathrm{d}} \frac{\pi d_{\mathrm{p}}^2}{4} = \left(\frac{32 l_{\mathrm{p}}}{d_{\mathrm{p}}^2} + \frac{6\pi}{d_{\mathrm{p}}} \right) \mu_{\mathrm{d}} u_{\mathrm{d}} \tag{5}$$

where l_{p} is the length of the pore channel, μ_{d} is the viscosity of the dispersed phase, and u_{d} is the dispersed phase flow velocity in the pore channel. The interfacial tension caused pressure could be expressed by the Young–Laplace equation:

$$\Delta p_{\mathrm{YL}} = \frac{4\gamma}{d_{\mathrm{drop}}} \tag{6}$$

where γ is the interfacial tension between the two liquid phases and d_{drop} is the drop diameter. The capillary pressure could also be expressed by the Young-Laplace equation:

$$\Delta p_{\mathrm{c}} = \frac{4\gamma \cos\theta}{d_{\mathrm{p}}} \tag{7}$$

where θ is the contact angle between the dispersed phase and the channel wall in the continuous phase ambient. Cos θ is taken to be 1, because for a pore with straight edges, the pressure inside the forming droplet is maximal when the droplet is hemispherical.

The drop formation process through the pore array is complicated. As shown in Figure 4a, the pores should be identified when the dispersed phase is pressed through them. However, drops from some pores may come out earlier than others due to some disturbance, as shown in Figure 4b. In this case, the resistances of pore 1 and 2 become smaller than that of pore 3 ($\Delta p_{\mathrm{YL}} < \Delta p_{\mathrm{c}}$) and the dispersed phase go through pore 1 and 2 more than pore 3. When the drops from pore 1 and 2 grow up as shown in Figure 4c, the flow rate in pore 3 become very small and the pore resistance is mainly provided by the capillary pressure. Then, whether pore 3 is active or not is decided by the pressure relationship in Figure 4c. Pore 3 is active only in the condition that

$$\Delta p_{\mathrm{f}} + \Delta p_{\mathrm{YL}} > \Delta p_{\mathrm{c}}. \tag{8}$$

When the droplet on a pore is break off, the pore activity will be decided by the flow conditions of other pores. Therefore, the active pores are random.

Submitting Eqs. 5–8, we have

$$Ca_{\mathrm{d}} > \frac{\left(1 - \frac{d_{\mathrm{p}}}{d_{\mathrm{drop}}}\right)}{\left(\frac{8 l_{\mathrm{p}}}{d_{\mathrm{p}}} + \frac{3\pi}{2}\right)} \tag{9}$$

where $Ca_{\mathrm{d}} = \frac{\mu_{\mathrm{d}} u_{\mathrm{d}}}{\gamma}$ is the capillary number of the dispersed phase. We define the right side of Eq. 9 as the critical capillary number of the dispersed phase, $Ca_{\mathrm{d}}^{(\mathrm{c})}$. The corresponding dispersed phase flow velocity is defined as the critical flow velocity, $u_{\mathrm{d}}^{(\mathrm{c})}$. The actual flow velocity of the dispersed phase in the pore channel is no smaller than the critical velocity. Otherwise, some pores will become inactive because of the low pore resistance pressure. On the other hand, the actual flow velocity of the dispersed phase is no bigger than the critical velocity when the active pore percentage is smaller than 100%. Therefore, the actual flow velocity of the dispersed phase is just the critical flow velocity when $\eta < 1$. This is why Eq. 2 fits the experimental data in Figure 3 well.

We can also calculate the theoretical value of $u_{\mathrm{d}}^{(\mathrm{c})}$ from Eq. 9. l_{p} is 0.5 mm and d_{p} is 0.18 mm as shown in Figure 1c. μ_{d} is 1×10^{-3} Pa s at 20°C, and γ is $\sim 1 \times 10^{-3}$ N/m, which is measured by the pendant drop method. The droplet diameter d_{drop} can be calculated based on the torque balance equation[39]

$$(F_{\gamma} - F_{\mathrm{stat}} - F_{\mathrm{BG}} - F_{\mathrm{D}}) d_{\mathrm{p}} = F_{\mathrm{R}} d_{\mathrm{drop}}. \tag{10}$$

Herein, F_{γ} is interfacial tension force, F_{stat} is static pressure difference force, F_{BG} is buoyancy force, F_{D} is dynamic lift force, and F_{R} is crossflow drag force. The detail of their

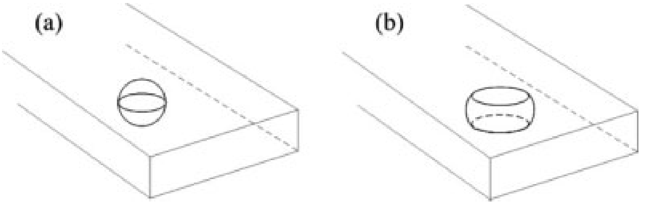

Figure 5. Flow patterns in the pore array microstructured device.

(a) Drop flow, (b) Disk flow.

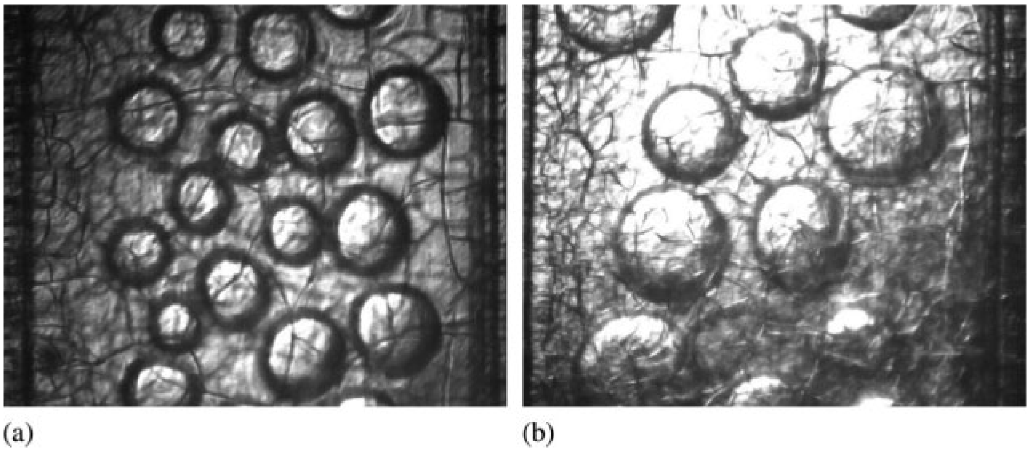

Figure 6. CCD images for drop flow and disk flow in the 3 × 3 pore array microstructured device.

(a) $Q_c = 500$ µl/min, $Q_d = 250$ µl/min, $C_c = 0.4$ mol/l, $C_d = 0.4$ mol/l. (b) $Q_c = 500$ µl/min, $Q_d = 250$ µl/min, $C_c = 0.1$ mol/l, $C_d = 0.2$ mol/l.

expression could be found in our previous work.[39] The calculated droplet diameter is ~0.45 mm and is consistent with our experimental measurement. Using these data, the calculated $u_d^{(c)}$ from Eq. 9 is 0.022 m/s, which is very close to the fitting result 0.021m/s.

Flow patterns

As illustrated by Figure 5, there are two different flow patterns in the pore array microstructured device, i.e., drop flow and disk flow. This is different from the T-junction microchannel flow, where the flow patterns are drop flow and plug flow. Figure 6 shows the CCD images for the samples of the drop flow and disk flow. However, we can not distinguish the two patterns from the CCD images directly because droplets in both of them are shown as circles. We distinguish the two flow patterns by comparing the circle diameter d_{drop} with the main channel height h. If $d_{\mathrm{drop}} > h$, the flow pattern is disk flow, otherwise it is drop flow. Therefore, the droplet sizes were measured using the CCD images.

Figure 7 shows the droplet sizes in both of the microstructured devices under different operation conditions. We can see from Figure 7a that the droplet size decreases with the continuous phase flow rate increasing. And the flow pattern turns from disk to drop. This phenomenon is because of the shear force increasing and is consistent with the results obtained in the T-junction microchannel.[37,40,41] Figure 7b shows that the dispersed flow rate has little effect on the droplet size in the experiments. The reason is that the actual flow velocity of the dispersed phase remains a constant at $u_d^{(c)}$ when the dispersed phase flow rate is small, which has been described in Section 3.1.

Figures 7c, d indicate that the concentration of the two phases has obvious effect on the droplet size. The reason is that the concentration of the two phases affects the interfacial tension greatly. We have measured the interfacial tension for the similar system of this work using pendent drop method in our previous job. Figure 8 shows the results, where Figure 8b is just from the previous article.[37] The measured interfacial tension is not the exact one for the conditions in the microstructured device because the mass transfer speed and the reaction conditions are different. However, the measured interfacial tension is consistent with the results shown in Figures 7c, d. The increasing of the continuous phase concentration decreases the interfacial tension and causes the droplet size decreasing. When the dispersed phase concentration is changed, the interfacial tension as well as the droplet size have a minimum value at the condition $C_d = 0.2$ mol/l.

The possible mechanisms of the influence of the two phase concentration on the flow patterns could be explained based on the measured interfacial tension. The increase of the sulfuric acid concentration leads to the increase of the mass transfer from the continuous phase to the dispersed phase, which results in the decrease of the interfacial tension. Therefore, the droplet size is decreased when the sulfuric acid concentration is increased. Because the chemical reaction is in the dispersed phase, so the amount of mass transfer is not influenced directly by the concentration of the dispersed phase. But the chemical reaction should enhance the mass transfer rate, which will influence the interfacial tension too. The interfacial tension first decreases with the dispersed phase concentration increasing because of the mass transfer enhancement, and then increases because of the salt-out effect. When the salt-out effect dominants the process, the droplet size will increase with the dispersed phase concentration increasing.

As an approximate treating, the measured interfacial tension in Figure 8 is used to the flow pattern partition in the following text. The apparent capillary numbers of both the phases, $Ca_c^{(a)}$ and $Ca_d^{(a)}$, which are defined as

$$Ca_c^{(a)} = \frac{\mu_c u_c^{(a)}}{\gamma} \tag{11}$$

and

$$Ca_d^{(a)} = \frac{\mu_d u_d^{(a)}}{\gamma}, \tag{12}$$

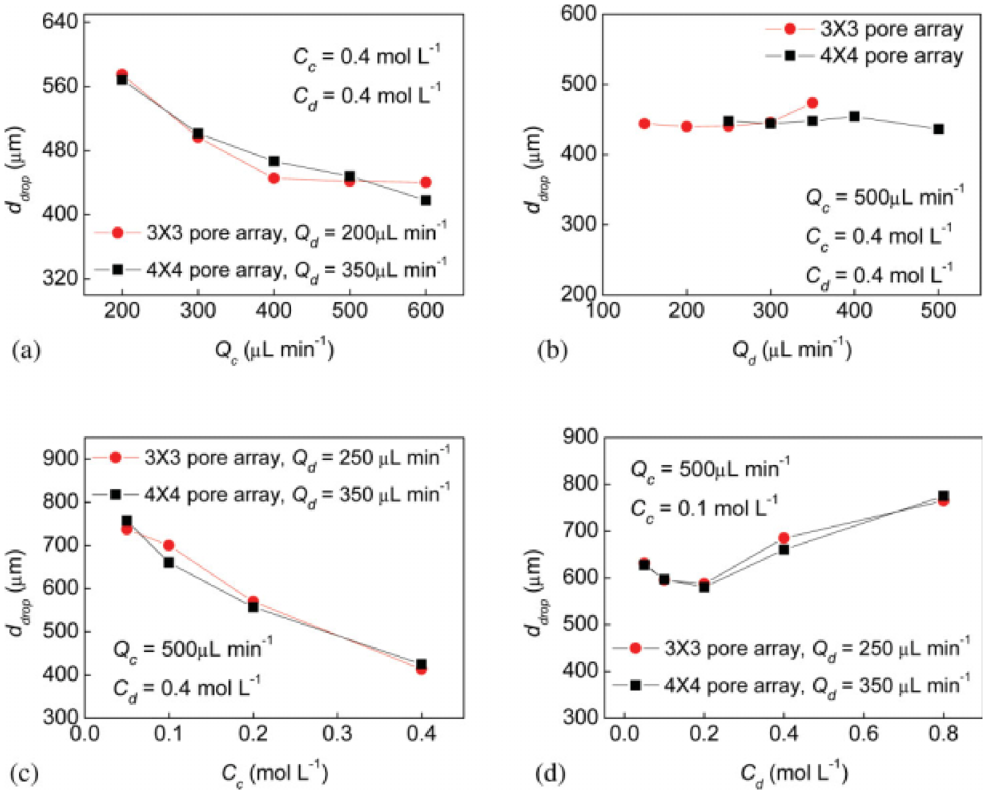

Figure 7. Operation condition effect on droplet size.

(a) Continuous phase flow rate effect on droplet size. (b) Dispersed phase flow rate effect on droplet size. (c) Continuous phase concentration effect on droplet size. (d) Dispersed phase concentration effect on droplet size. [Color figure can be viewed in the online issue, which is available at www.interscience.wiley.com.]

are calculated in different experiment conditions. Herein, $u_c^{(a)} = \frac{Q_c}{S}$ is the apparent flow velocity of the continuous phase. S is the cross section area of the main channel. With $Ca_c^{(a)}$ as the abscissa and $Ca_d^{(a)}$ as the ordinate, the experiment results are marked in one chart as shown in Figure 9. The data spots are distinctly separated into two different groups by the solid line in the figure. With high apparent capillary number of the continuous phase, the flow pattern is drop flow. This result is consistent with the literature.[22,41] However, the apparent capillary number of the dispersed phase has little effect on the flow pattern. The reason is that the active pore percentage in most of our experiment conditions is below 100% and actual velocity of the dispersed phase is not changed.

Particle size

The particle size in a precipitation process is basically decided by the competition of nucleation and growth, which are controlled by the system supersaturation ratio. High supersaturation ratio generates small particles for a short nucleation burst while low supersaturation ratio generates larger ones for persistent particle growth.[25–30] The

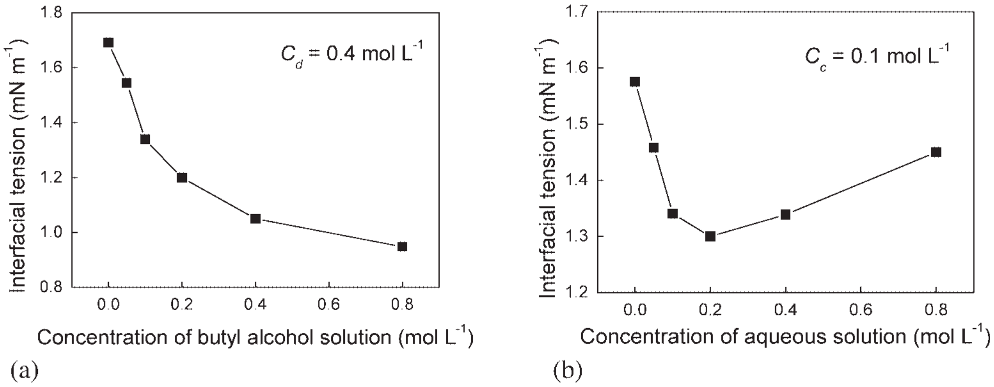

Figure 8. Interfacial tension between the butyl alcohol solutions and the aqueous solutions.

(a) Continuous phase concentration effect on interfacial tension. (b) Dispersed phase concentration effect on interfacial tension.[37]

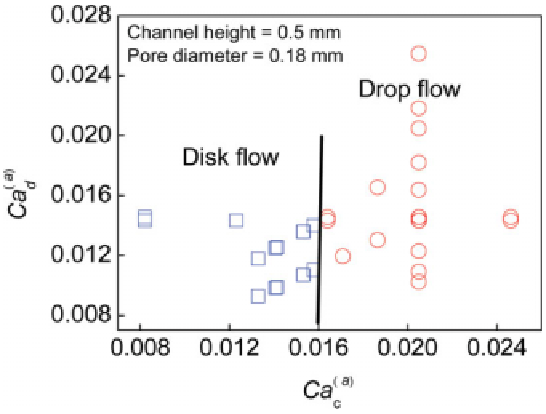

Figure 9. Flow pattern partition in the pore array microstructured device.

[Color figure can be viewed in the online issue, which is available at www.interscience.wiley.com.]

precipitation takes place in the droplets in our experiments and the supersaturation ratio is determined by the initial concentration, flow pattern, as well as the mass transfer speed.

$BaSO_4$ nanoparticles with size between 10 nm and 30 nm were successfully produced with the two phase flow in our experiment. Some of the TEM pictures are shown in Figure 10. We could see that the particle size varies obviously when the experimental conditions are changed. The prepared nanoparticles show good monodispersity. Comparing with our previous work,[37] the particle size and monodispersity in this work are similar with the nanoparticles produced in the T-junction microchannel. This result proves that the scaling up from T-junction microchannel to pore array microstructured devices is successful. Pore number in this work shows little effect on the flow and the producing particles, which indicates the further developing potential of this scaling up strategy.

If the flow patterns are similar, i.e., with similar droplet size, the initial concentration decides the supersaturation ratio. Therefore, high initial concentration generates small particles. Figures 10a, b show an example for this situation. The droplet sizes of these pictures are similar. We can see that the particle size of Figure 10a is smaller than that of Figure 10b, while the concentrations of both phases are bigger in Figure 10a.

If the two phase flow has different flow pattern or different droplet size, the nanoparticle size will be different even at same initial concentration. Figures 10c, d show an example for this situation. We can see that the particle size decreases with the increase of the droplet size at same initial concentration. This phenomenon indicates that big droplet size is benefit to nucleation rather than growth.

To know about the relationship between the droplet size and the nanoparticle size, we plot all the results of particle size and droplet size in one picture, as shown in Figure 11. We call this figure the particle size diagram.

In the particle size diagram, the abscissa is droplet size. The ordinate is the particle size. We can see clearly that the particle size decreases with the increase of droplet size in both the drop flow region and the disk flow region while it has a reverse changing trend in the transition region. The data spots distribute within a narrow belt marked in the diagram. The slope of the belts characterizes the effect of the droplet size on particle size while the width of the belts characterizes the effect of the initial concentration. Of course, as shown in Figures 7c, d, the initial concentration

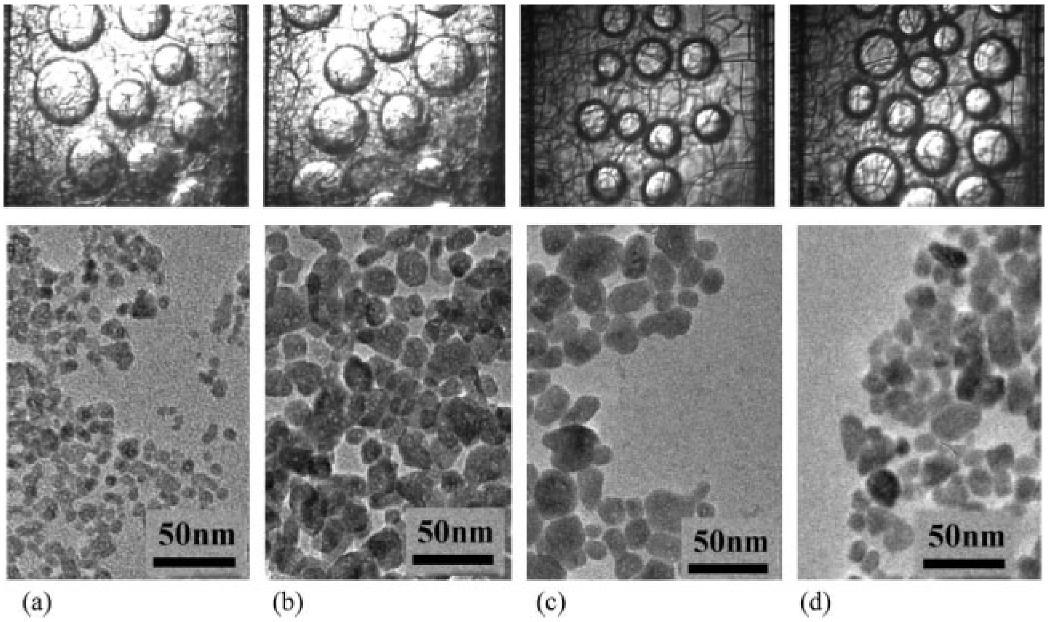

Figure 10. Flow images and the corresponding particles with different experiment conditions in the 3 × 3 pore array microstructured device.

(a) $C_c = 0.2$ mol/l, $C_d = 0.4$ mol/l, $Q_c = 500$ μl/min, $Q_d = 250$ μl/min. (b) $C_c = 0.1$ mol/l, $C_d = 0.2$ mol/l, $Q_c = 500$ μl/min, $Q_d = 250$ μl/min. (c) $C_c = 0.4$ mol/l, $C_d = 0.4$ mol/l, $Q_c = 500$ μl/min, $Q_d = 150$ μl/min. (d) $C_c = 0.4$ mol/l, $C_d = 0.4$ mol/l, $Q_c = 500$ μl/min, $Q_d = 350$ μl/min.

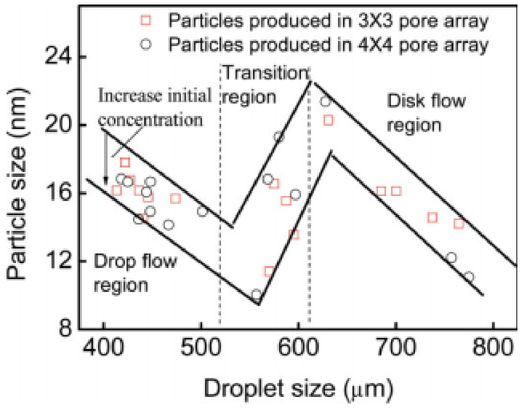

Figure 11. Particle size diagram.

[Color figure can be viewed in the online issue, which is available at www.interscience.wiley.com.]

has a great influence on the flow patterns and the droplet size.

Although it is hard to explain the diagram clearly, we would like to explain the possible reasons for our experimental results. The particle size difference in different flow patterns and droplet sizes may be explained by the forming mechanism of two-phase regular flow and the mass transfer speed.

Each process in the pore-array microstructured device is a combination of some of the four steps shown in Figure 12. For example, the drop flow process is composed of Steps 1 and 2; the disk flow process is composed of Steps 1, 3, and 4. Each step has different mass transfer speed. In Step 1, the drop generating stage, there is a strong inner circulatory flow inside drops because of the action of shear force of the continuous phase, and the mass transfer speed inside drops is very high. Some experiments in microchannel have shown that 70% of the total mass transfer could be accomplished during the drop generating stage.[42] The supersaturation ratio will be very high due to the high mass transfer speed. We can approximately estimate this supersaturation ratio based on the following expression

$$S = \gamma_{\pm}\sqrt{\frac{C_c C_d}{K_{sp}}}, \tag{13}$$

where $\gamma_{\pm}$ is a function of the ionic strength and in the range of 0.1–1. K_{sp} is the solubility product, which takes the value of 1.08×10^{-4} mol^2/m^6 at 25°C.[30] With this estimation, we can know that the supersaturation ratio around the interface is in the range of 10^3–10^4 and homogenous nucleation will mainly take place at this high supersaturation ratio. A large amount of reactants react at Step 1 because of the nucleation. In Step 2, the flowing of the drops in the main channel, the inner circulatory flow is weak and diffusion is the main mass transfer approach.[43] In this case, the mass transfer speed is low and the supersaturation ratio will fall down quickly. Growth will mainly take place in this step. In Step 3, when the droplet size reaches the channel height in the drop formation process, the inner flow of the drop is weakened by the top wall of the main channel and the mass transfer speed is low. The supersaturation ratio will fall down. In Step 4, the flowing of the disks, there are strong internal circulations in both the aqueous and oil phase because of the friction of the channel wall. Similar phenomenon was reported as slug flow in microchannels.[4] Therefore, the mass transfer between the two phases is highly enhanced. The supersaturation ratio will rise up when the disk is break off from the dispersed pore. Then, the supersaturation ratio will fall down after it reaches a maximum value because of the consumption of the materials.

On the basis of the above analysis, the supersaturation ratio changing with time for the drop flow can be sketched by Figure 13. We can see clearly there are two steps in the curves corresponding to Steps 1 and 2, respectively. Nucleation and growth are, respectively, the main process for these two steps. If the drop size is bigger, Step 1 will take longer time and nucleation stage will be longer.

For the disk flow, the supersaturation ratio changing can be sketched by Figure 14. The curve could be disparted into four parts. The first two parts are corresponded to Step1 and 3 in Figure 12, respectively. The last two parts are corresponded to Step 4 in Figure 12. If the disk size is bigger, the material infused into the disk in Step 3 will cause a higher rise of the supersaturation ratio in Step 4.

For comparison of different flow conditions, we plot the supersaturation ratio changing curves for different droplet sizes in one chart as shown in Figure 15. For curves (I) to (V), the droplet size gets bigger and turns from drop to disk. (I) and (II) are for drop flow while (IV) and (V) are for disk flow.

Comparing with curve (I), which denotes smaller drops, the drop formation time for curve (II) is longer. Therefore, the nucleation process persists a longer time and consumes most of the reactants. The materials left for the later growth stage become less and the finally produced particles are smaller. We could quantitatively describe this process with some approximate assumption. In curves (I) and (II), the supersaturation ratio in Step 1 is not constant. However, it experiences a slowly dropping stage. The reason is that the continuous flow washes the surface of the droplet and the concentration of the sulfuric acid at the interface almost

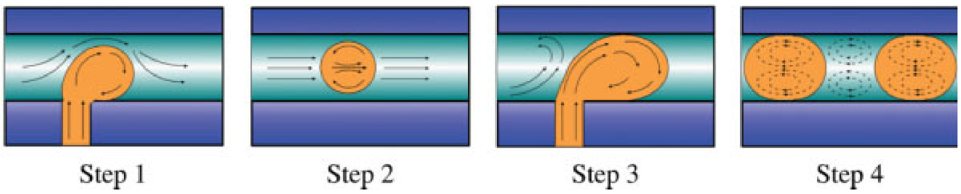
Step 1 Step 2 Step 3 Step 4

Figure 12. Different steps in the drop and disk flow process.

[Color figure can be viewed in the online issue, which is available at www.interscience.wiley.com.]

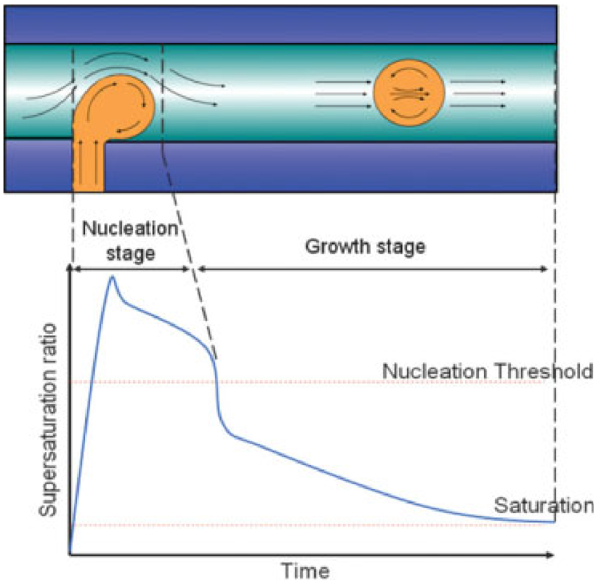

Figure 13. Supersaturation ratio vs. time for drop flow.

[Color figure can be viewed in the online issue, which is available at www.interscience.wiley.com.]

remains constant. On the other hand, the inner circulatory flow inside drops is very strong and the new injected barium chloride is fast taken to the reaction area, which makes the supersaturation ratio dropping slower. Because the supersaturation ratio changes slowly in this stage, we can use an average value for approximate calculating. Moreover, the average value for curve (I) and (II) in Step 1 is approximately equal. Therefore, we can use the same average supersaturation ratio for drops with different sizes. With the average supersaturation ratio, nucleation rate can be calculated. As the thickness of the reaction area around the interface changes little, we use the interface nucleation rate J (m^2/s) instead of the volumetric nucleation rate to make the calculation easier. The generated nuclei number in an infinitesimal time dt is $dN = JA\ dt$, where A is the interface area of a drop. Assuming the drop is spherical, we have $A = 4\pi r^2$. The volume of the drop is $V = \frac{Q_\mathrm{d}}{\eta n} t = \frac{4}{3}\pi r^3$, and thus $dt = \frac{4\pi\eta n\, r^2}{Q_\mathrm{d}} dr$. Then we have $dN = \frac{16\pi^2 \eta n J r^4}{Q_\mathrm{d}} dr$. Integrating this expression, we can obtain the nuclei number generated in a drop with radius R, $N = \frac{16\pi^2 \eta n J R^5}{5Q_\mathrm{d}}$. Then the mean volume value of particles generated in drops with radii R is $V_\mathrm{p} = \frac{VC_\mathrm{d}M}{\rho N} = \frac{5Q_\mathrm{d}C_\mathrm{d}M}{12\pi\eta n\, \rho J R^2}$, where V is the volume of drop, M and ρ are respectively the molar mass and density of barium sulfate. The mean particle size $d_\mathrm{p} \sim R^{-2/3}$, i.e., the particle size decreases with the drop size increasing.

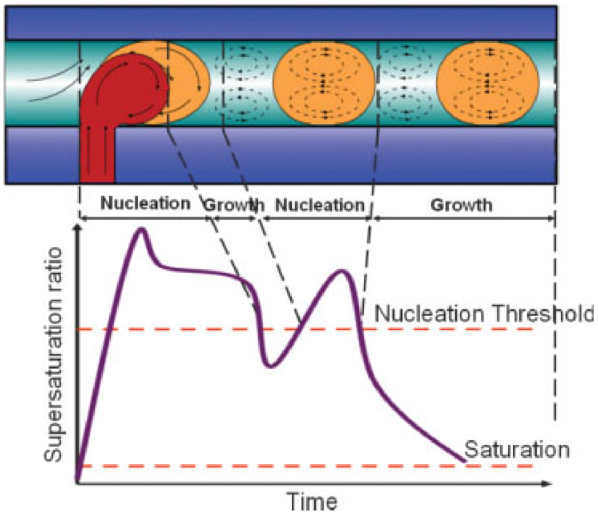

Figure 14. Supersaturation ratio vs. time for disk flow.

[Color figure can be viewed in the online issue, which is available at www.interscience.wiley.com.]

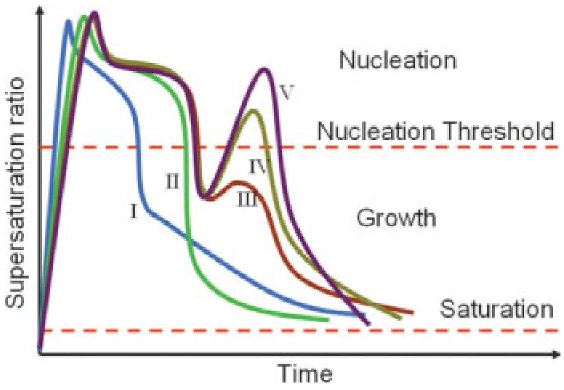

Figure 15. Supersaturation ratio vs. time in different flow patterns.

(I), (II) drop flow and the drop size of (I) is smaller; (III) transition flow; (IV), (V) disk flow and the disk size of (IV) is smaller. [Color figure can be viewed in the online issue, which is available at www.interscience.wiley.com.]

In the transition flow, the supersaturation ratio changing is similar to Figure 14. But the supersaturation ratio rise after Step 3 is smaller because of the smaller disk size, which could be seen from curve (III) in Figure 15. Because the material injected into the droplet in Step 3 is mainly used for the particle growth, the particle size increases with the droplet size increasing in this region.

Comparing with curve (III), the disk for curves (IV) and (V) is big enough and the supersaturation ratio in Step 4 rises above the nucleation threshold. The once more nucleation will cause a decrease of the particle size. In this region, bigger disks have longer nucleation stage and consume more of the reactants. The materials left for the growth become less and the finally produced particles are smaller. This can also be observed from the comparison of curve (IV) and (V) in Figure 15.

Conclusions

As a scaling up strategy based on the T-junction microchannel, $BaSO_4$ nanoparticle producing reaction system was investigated in the pore array microstructured devices. Nanoparticles with size between 10 nm and 30 nm were produced through the liquid–liquid two-phase flow in the devices. By adjusting the experimental conditions including the two phase concentrations and flow rates, droplets with different shapes and sizes were generated in the microstructured devices and the size of $BaSO_4$ nanoparticles was controlled. Mass transfer and chemical reaction could affect the interfacial tension and flow patterns seriously. With the interfacial tension measured in different concentrations, a picture distinguishing the two-phase flow patterns, i.e., the drop flow and the disk flow, was plotted. The experimental results showed that the particle size decreased with the increasing of droplet size in both the drop flow region and the disk flow region while it had a reversed trend in the transition region. The mechanisms have been provided to explain the effect of flow patterns.

Acknowledgments

The authors acknowledge the supports of the National Natural Science Foundation of China (20476050 and 20525622) and National Basic Research Program of China (2007CB714302) on this work gratefully.

Notation

A = interface area of a drop (mm^2)
$Ca_c^{(a)}$ = apparent capillary number of the continuous phase
Ca_d = capillary number of the dispersed phase
$Ca_d^{(a)}$ = apparent capillary number of the dispersed phase
$Ca_d^{(c)}$ = critical capillary number of the dispersed phase
C_c = concentration of continuous phase (mol/l)
C_d = concentration of dispersed phase (mol/l)
J = interface nucleation rate (mm^2/s)
M = molar mass of barium sulfate (g/mol)
N = nuclei number or particle number in one droplet
Q_c = flow rate of continuous phase (μl/min)
Q_d = flow rate of dispersed phase (μl/min)
R = final droplet radius (mm)
S = cross section area of the main channel (mm^2)
V = droplet volume (mm^3)
V_p = particle volume (mm^3)
d_{drop} = the drop diameter (μm)
d_p = pore diameter (mm)
l_p = length of pore channel (mm)
n = pore number
Δp_c = capillary pressure (Pa)
Δp_f = pore resistance caused pressure (Pa)
Δp_{YL} = interfacial tension caused pressure (Pa)
r = variable droplet radius (mm)
$u_c^{(a)}$ = apparent flow velocity of the continuous phase (m/s)
u_d = actual flow velocity of the dispersed phase (m/s)
$u_d^{(a)}$ = apparent flow velocity of the dispersed phase (m/s)
$u_d^{(c)}$ = critical flow velocity of the dispersed phase (m/s)
γ = interfacial tension (N/m)
η = active pore percentage (%)
θ = contact angle
μ_c = viscosity of the continuous phase (Pa s)
μ_d = viscosity of the dispersed phase (Pa s)
ρ = density of barium sulfate (g/cm^3)

Literature Cited

1. Ehrfeld W, Hessel V, Löwe H. *Microreactors: New Technology for Modern Chemistry*. Weinheim: Wiley-VCH, 2000.
2. Pamme N. Continuous flow separations in microfluidic devices. *Lab Chip*. 2007;7:1644–1659.
3. Song H, Chen DL, Ismagilov RF. Reactions in droplets in microfluidic channels. *Angew Chem Int Ed*. 2006;45:7336–7356.
4. Burns JR, Ramshaw C. The intensification of rapid reactions in multiphase systems using slug flow in capillaries. *Lab Chip*. 2001; 1:10–15.
5. Burns JR, Ramshaw C. A microreactor for the nitration of benzene and toluene. *Chem Eng Commun*. 2002;189:1611–1628.
6. Dittrich PS, Tachikawa K, Manz A. Micro toal analysis systems, latest advancements. *Trends Analyt Chem*. 2006;78:3887–3908.
7. Xu JH, Luo GS, Chen GG, Tan B. Mass transfer performance and two-phase flow characteristic in membrane dispersion mini-extractor. *J Memb Sci*. 2005;249:75–81.
8. Kumemura M, Korenaga T. Quantitative extraction using flowing nano-liter droplet in microfluidic system. *Anal Chim Acta*. 2006; 558:75–79.
9. Grodrian A, Metze J, Henkel T, Martin K, Roth M, Kohler JM. Segmented flow generation by chip reactors for highly parallelized cell cultivation. *Biosens Bioelectron*. 2004;19:1421–1428.
10. Zheng B, Tice JD, Ismagilov RF. Formation of droplets of in microfluidic channels alternating composition and applications to indexing of concentrations in droplet-based assays. *Anal Chem*. 2004;76: 4977–4982.
11. Steinbacher JL, McQuade DT. Polymer chemistry in flow: new polymers, beads, capsules, and fibers. *J Polym Sci Part A: Polym Chem*. 2006;44:6505–6533.
12. Zourob M, Mohr S, Mayes AG, Macaskill A, Pérez-Moral N, Fielden PR, Goddard NJ. A micro-reactor for preparing uniform molecularly imprinted polymer beads. *Lab Chip*. 2006;6: 296–301.
13. Nie Z, Xu S, Seo M, Lewis PC, Kumacheva E. Polymer particles with various shapes and morphologies produced in continuous microfluidic reactors. *J Am Chem Soc*. 2005;127:8058–8063.
14. Quevedo E, Steinbacher J, McQuade DT. Interfacial polymerization within a simplified microfluidic device: capturing capsules. *J Am Chem Soc*. 2005;127:10498–10499.
15. Dendukuri D, Tsoi K, Hatton TA, Doyle PS. Controlled synthesis of nonspherical microparticles using microfluidics. *Langmuir*. 2005; 21:2113–2116.
16. Dendukuri D, Pregibon DC, Collins J, Hatton TA, Doyle PS. Continuous-flow lithography for high-throughput microparticle synthesis. *Nat Mater*. 2006;5:365–369.
17. Khan SA, Günther A, Schmidt MA, Jensen KF. Microfluidic synthesis of colloidal silica. *Langmuir*. 2004;20:8604–8611.
18. Yen BKH, Günther A, Schmidt MA, Jensen KF, Bawendi MG. A microfabricated gas-liquid segmented flow reactor for high-temperature synthesis: the case of CdSe quantum dots. *Angew Chem Int Ed*. 2005;44:5447–5451.
19. Hung LH, Tseng WY, Choi K, Tan YC, Shea KJ, Lee AP. Controlled droplet fusion in microfluidic devices. Eighth International Conference on MicroTAS. Malmo, Sweden. 2004;2:539–541.
20. Sotowa KI, Irie K, Fukumori T, Kusakabe K, Sugiyama S. Droplet formation by the collision of two aqueous solutions in a microchannel and application to particle synthesis. *Chem Eng Technol*. 2007; 30:383–388.
21. Shestopalov I, Tice JD, Ismagilov RF. Multi-step synthesis of nanoparticles performed on millisecond time scale in a microfluidic droplet-based system. *Lab Chip*. 2004;4:316–321.
22. Günther A, Jensen KF. Multiphase microfluidics: from flow characteristics to chemical and materials synthesis. *Lab Chip*. 2006;6: 1487–1503.
23. Chan EM, Alivisatos AP, Mathies RA. High-temperature microfluidic synthesis of CdSe nanocrystals in nanoliter droplets. *J Am Chem Soc*. 2005;127:13854–13861.
24. Siegel RW. Creating nanophase materials. *Sci Am*. 1996;275:74–79.
25. Li SW, Xu JH, Luo GS. Control of crystal morphology through supersaturation ratio and mixing conditions. *J Cryst Growth*. 2007; 304:219–224.
26. Chen GG, Luo GS, Xu JH, Wang JD. Membrane dispersion precipitation method to prepare nanoparticles. *Powder Tech*. 2004;139: 180–185.
27. La Mer VK, Dinegar RH. Theory, production and mechanism of formation of monodispersed hydrosols. *J Am Chem Soc*. 1950;72: 4847–4854.
28. Mantzaris NV. Liquid-phase synthesis of nanoparticles: particle size distribution dynamics and control. *Chem Eng Sci*. 2005;60:4749–4770.
29. Gradl J, Schwarzer HC, Schwertfirm F, Manhart M, Peukert W. Precipitation of nanoparticles in a T-mixer: coupling the particle population dynamics with hydrodynamics through direct numerical simulation. *Chem Eng Proc*. 2006;45:908–916.
30. Schwarzer HC, Peukert W. Tailoring particle size through nanoparticle precipitation. *Chem Eng Commun*. 2004;191:580–606.

31. Sugiura S, Nakajima M, Seki M. Prediction of droplet diameter for microchannel emulsification. *Langmuir*. 2002;18:3854–3859.
32. Sugiura S, Nakajima M, Kumazawa N, Iwamoto S, Seki M. Characterization of spontaneous transformation-based droplet formation during microchannel emulsification. *J Phys Chem B*. 2002;106: 9405–9409.
33. Geerken MJ, Lammertink RGH, Wessling M. Interfacial aspects of water drop formation at micro-engineered orifices. *J Colloid Interface Sci*. 2007;312:460–469.
34. Kobayashi I, Nakajima M, Mukataka S. Preparation characteristics of oil-in-water emulsions using differently charged surfactants in straight-through microchannel emulsification. *Colloid Surf A Physicochem Eng Asp*. 2003;229:33–41.
35. Kobayashi I, Mukataka S, Nakajima M. Effect of slot aspect ratio on droplet formation from silicon straight-through microchannels. *J Colloid Interface Sci*. 2004;279:277–280.
36. Kobayashi I, Mukataka S, Nakajima M. Novel asymmetric through-hole array microfabricated on a silicon plate for formulating monodisperse emulsions. *Langmuir*. 2005;21:7629–7632.
37. Li SW, Xu JH, Wang YJ, Luo GS. Controllable preparation of nanoparticles by drops and plugs flow in a microchannel device. *Langmuir*. 2008;24:4194–4199.
38. Gijsbertsen-Abrahamse AJ, van der Padt A, Boom RM. Influence of membrane morphology on pore activation in membrane emulsification. *J Memb Sci*. 2003;217:141–150.
39. Xu JH, Luo GS, Chen GG, Wang JD. Experimental and theoretical approaches on droplet formation from a micrometer screen hole. *J Memb Sci*. 2005;266:121–131.
40. Xu JH, Li SW, Tan J, Wang YJ, Luo GS. Preparation of highly monodisperse droplet in a T-junction microfluidic device. *AIChE J*. 2006;52:3005–3010.
41. Xu JH, Luo GS, Li SW, Chen GG. Shear force induced monodisperse droplet formation in a microfluidic device by controlling wetting properties. *Lab Chip*. 2006;6:131–136.
42. Xu JH, Tan J, Li SW, Luo GS. Enhancement of mass transfer performance of liquid–liquid system by droplet flow in microchannels. *Chem Eng J*. 2008;141:242–249.
43. Mary P, Studer V, Tabeling P. Microfluidic droplet-based liquid–liquid extraction. *Anal Chem*. 2008;80:2680–2687.

Manuscript received Nov. 16, 2008, and revision received Mar. 23, 2009.